

---

# DO MACHINES FAIL LIKE HUMANS? A HUMAN-CENTRED OUT-OF-DISTRIBUTION SPECTRUM FOR MAPPING ERROR ALIGNMENT

---

**Binxia Xu**  
School of Data Science  
Fudan University  
Shanghai  
binxia\_xu@fudan.edu.cn

**Xiaoliang Luo**  
London  
xiao.luo.17@ucl.ac.uk

**Luke Dickens**<sup>†</sup>  
Department of Information Studies  
University College London  
London  
l.dickens@ucl.ac.uk

**Robert M. Mok**<sup>†</sup>  
Center for Information and Neural Networks  
National Institute of Information and  
Communications Technology  
University of Osaka  
Osaka  
rob.mok@nict.go.jp

## ABSTRACT

Determining whether AI systems process information similarly to humans is central to cognitive science and trustworthy AI. While modern AI models match human accuracy on standard tasks, such parity does not guarantee that their underlying decision-making strategies are aligned with human information processing. Assessing performance using i) error alignment metrics to compare how humans and models fail, and ii) using distorted, or otherwise more challenging, stimuli, provides a viable pathway toward a finer characterization of model-human alignment. However, existing out-of-distribution (OOD) analyses for challenging stimuli are limited due to methodological choices: they define OOD shift relative to model training data or use arbitrary distortion-specific parameters with little correspondence to human perception, hindering principled comparisons. We propose a human-centred framework that redefines the degree of OOD as a spectrum of human perceptual difficulty. By quantifying how much a collection of stimuli deviates from an undistorted reference set based on human accuracy, we construct an OOD spectrum and identify four distinct regimes of perceptual challenge. This approach enables principled model-human comparisons at calibrated difficulty levels. We apply this framework to object recognition and reveal unique, regime-dependent model-human alignment rankings and profiles across deep learning architectures. Vision-language models are the most consistently human aligned across near- and far-OOD conditions, but CNNs are more aligned than ViTs for near-OOD and ViTs are more aligned than CNNs for far-OOD conditions. Our work demonstrates the critical importance of accounting for cross-condition differences such as perceptual difficulty for a principled assessment of model-human alignment.

**Keywords** Error alignment · Human-centred OOD

## 1 Introduction

Evaluating whether artificial intelligence systems process information in ways comparable to humans is a fundamental challenge for both cognitive science and computer science. From a cognitive science perspective, neural network models

---

<sup>†</sup>Equal senior authorship contribution.

Do machines fail like humans?

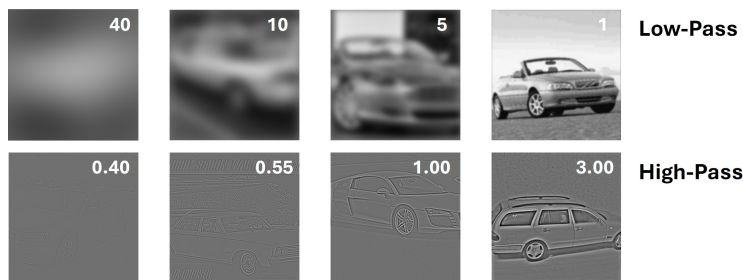


Figure 1: Example images from two distortion types (low-pass and high-pass filtering) from the *modelvshuman* dataset [22] at different parameter levels. Images within the same column share the same parameter rank within each distortion type.

offer computational abstractions of hypothesised mechanisms underlying human information processing [1, 2, 3], and assessing their alignment with humans provides a systematic way to test these hypotheses [4, 5]. From a computer science perspective, models whose information processing reflects human cognition may exhibit greater robustness [6, 7], interpretability [8, 9], and trustworthiness [10, 11]. As humans generalise remarkably well across diverse and imperfect environments, models that better reflect human processing principles may inherit similar robustness properties. Existing AI models achieve or exceed human accuracy on clear inputs. However, human-level accuracy does not entail model-human alignment, as systems may make markedly different errors reflecting different processing mechanisms. Thus, going beyond accuracy is crucial [12, 4]. Metrics such as error consistency (EC)[13] and misclassification agreement (MA)[14] address this by measuring error patterns between systems. Yet comparing errors on easy tasks is insufficient – alignment may appear high on clear stimuli simply due to the infrequency of errors. Challenging conditions, where error patterns can become more distinct, are essential for rigorously assessing model-human alignment.

Although these considerations apply broadly, visual perception provides a particularly well-defined testbed for studying alignment under challenging conditions. When systems are exposed to degraded visual input, errors reveal inductive biases – the visual features they degrade reflecting their information-processing strategies [15, 16, 17]. Distortions that selectively disrupt edges, texture, global structure, or high-frequency detail differentially impair systems depending on which cues they privilege (e.g., texture or global shape). Researchers have sought to compare the behavioral patterns of humans and models under stimuli of different distortion types, which they call ‘out-of-distribution’ (OOD) samples [18, 19, 20, 21]. However, to assess model-human alignment appropriately, performance must be compared on a common and meaningful scale. We identify four fundamental problems for model-human comparison under distorted conditions and provide a human-centered behavioral deviation framework to solve these issues.

First, OOD has been defined based on models rather than humans. In machine learning, OOD is defined by deviation from training data statistics [23]. Recent work focuses on OOD samples for models [24, 21, 25]. However, for humans, this definition does not straightforwardly apply. Humans do not have a finite, controlled “training distribution,” but instead acquire visual knowledge through a lifetime of varied, naturally encountered experience. This asymmetry raises fundamental questions: Are OOD samples for models also OOD for humans? For instance, is Figure 1, OOD for humans? What does OOD mean for human perception, and how should it be defined?

Second, the level of degradation is typically defined by image-processing pipeline parameters rather than a universal measure. Consider the distortions in Figure 1. If we want to compare the impact of specific feature impairment, which conditions should we choose? Should we select those within the same column? If human perceptual difficulty varies across conditions it is unclear if differences in error patterns reflect feature or information-processing differences or difficulty. A low-pass filter with parameter 5 and a high-pass filter with parameter 1 cannot be meaningfully placed on a common scale, despite sharing the same parameter rank. Some studies aggregate performance across severity levels [21, 22, 14], but such an approach ignores how perceptual difficulty varies across a distortion type. Others qualitatively select distortion levels that appear roughly comparable [26, 19, 27, 28], but this introduces subjective judgement. Hendrycks et al. [21] normalised to a reference model (AlexNet [29]), but this substitutes one arbitrary reference for another where the resulting scale reflects the idiosyncrasies of that architecture rather than any principled notion about image degradation.

Third, not all degradation conditions are equally meaningful for the investigation. Consider an extreme example where an image with a low-pass parameter of 40 appears unrecognisable to humans (Figure 1) – would such a stimulus be appropriate for assessing model-human alignment? If not, how can we determine the appropriate stimulus set for each distortion type?

Do machines fail like humans?

Lastly, raw model-human alignment values can be misleading without a baseline. Previous work treats model-human alignment values directly as evidence of alignment [22]. However, this interpretation is incomplete without considering a baseline such as human–human alignment values. When humans show zero agreement on a stimulus set, we cannot expect high model-human alignment.

To address these challenges, we propose a **human-centred behavioral deviation framework** that provides a natural benchmark for fairly comparing model-human alignment across distortion types on a common scale. Rather than using distortion-specific parameters (Figure 1), we place them on a shared scale anchored in human perceptual difficulty (Figure 2B). We operationalise this using the effect size Glass’s  $\Delta$  [30] applied to accuracy logits – the deviation of human performance from undistorted stimuli, which we term the reference distribution. We refer to this quantity as **the OOD score**. With this, we redefine OOD for humans as deviation from this reference condition that impairs human perception in quantifiable, graded ways. Moreover, for cognitive science, defining OOD in terms of human perceptual difficulty provides a principled way to control task difficulty across conditions, enabling systematic investigation of individual differences in visual processing strategies that would be confounded by arbitrary distortion parameters [31].

Our analysis is conducted on the *modelvs-human* dataset [22], which contains human core object recognition performance on systematically distorted images. To preview the results, our approach reveals that a perceptual OOD spectrum contains distinct regions that reflect different regimes of human information processing. We evaluate models within near- and far-OOD regions, showing distinct model-human alignment patterns across regimes: Vision-Language Models (VLMs) [32] show the most consistent alignment across regimes, whereas Vision Transformer models (ViTs) [33] achieve higher alignment than Convolutional Neural Networks (CNNs) [34] in near-OOD but the reverse pattern for far-OOD. In sum, this work introduces a human-centred framework to appropriately compare human and model error profiles, and offer an empirical characterisation of how different model architectures align with human perception across regimes.

## 2 Results

### 2.1 Constructing an Out-of-Distribution (OOD) Spectrum Based on Human Perceptual Difficulty

#### 2.1.1 Human Behavior Shifts Under Distortions

To test whether distortions produce significant shifts in human recognition behavior, we compared the distribution of human accuracies under distortion for each condition (one condition refers to one level of one distortion type, four participants per condition) with the undistorted baseline (28 values in total) (Figure 2.A). We found that distorted images induced substantial shifts in behavior: only 7 out of 65 distortion conditions were not significantly different from the undistorted condition (Mann–Whitney U test:  $p < 0.01$ , False Discovery Rate corrected; see Table S2 in Appendix A for all results), and accuracy was significantly above chance in 54 of 65 conditions ( $P=1/16$  categories; one-tailed binomial tests, FDR corrected; see Table S3 for all results).

#### 2.1.2 Building the OOD Spectrum through Quantifying Human Performance Deviation

To build the perceptual OOD spectrum, we construct a reference distribution that quantifies how much each distorted condition deviates from the undistorted baseline (i.e., the effect size), providing a continuous measure of distortion severity grounded in human performance. Due to non-normality in the accuracy scores (Shapiro–Wilk test,  $p < 0.05$ ), we applied a logit transformation to the scores, after which all tests yielded  $p > 0.05$ , indicating no rejection of the null hypothesis of normality (see Appendix A, Table S4).

To characterize the distribution of human accuracy under distortion, we define an **OOD score** based on Glass’s  $\Delta$  as the measure for behavioral deviation:

$$\Delta = \frac{\bar{l}_d - \bar{l}_{ud}}{s_{ud}}, \quad (1)$$

where  $\bar{l}_d$  and  $\bar{l}_{ud}$  are the mean logit-transformed accuracies on the distorted set and undistorted set respectively, and  $s_{ud}$  is the standard deviation for the logit-transformed accuracy on the undistorted images. Glass’s  $\Delta$  is appropriate here because it standardises the mean difference between performance on distorted and undistorted images using only the reference condition’s variance, ignoring the variance of each distorted condition. This ensures comparability across conditions by measuring all deviations on a common scale defined by the reference – the baseline condition – and avoids underestimating behavioral differences for distortion conditions with high variance.

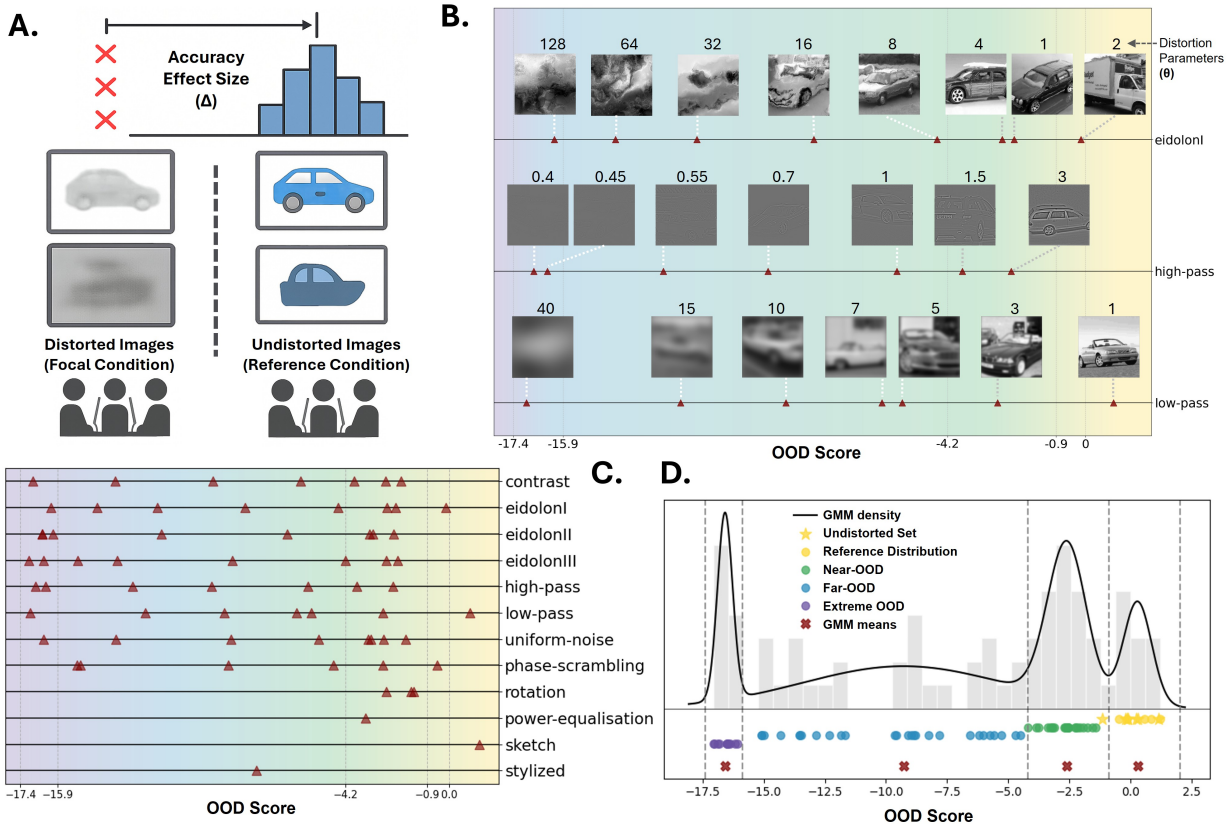


Figure 2: A human-centered OOD spectrum. (A) Illustration of the process for measuring the degree of human performance deviation on a specific distortion condition relative to undistorted images. (B) OOD spectrum constructed from human accuracy (logit transformed). The x-axis represents the OOD score, indicating the degree of deviation from the performance baseline on undistorted images, with greater negative values corresponding to larger distributional shifts. Example images from selected distortions are shown above their corresponding positions on the axis. (C) OOD scores for all levels of corruption for each distortion type in *modelvshuman* dataset. (D) Four-component Gaussian Mixture Model (GMM) fitted to OOD scores across all distortion conditions, defining the four OOD groups. Color reflects different OOD regimes. Boundaries illustrated by dashed lines.

### 2.1.3 The Perceptual Distortion OOD Spectrum

To meaningfully assess model robustness in relation to human perception, we construct a human-centred spectrum OOD based on behavioral deviation across distortion types and levels, which allows us to replace the arbitrary distortion parameter scales. To illustrate the range of behavioral deviation, we present three example distortion types (Figure 2.B). The behavioral deviation effect sizes for all distortion conditions are presented in Figure 2.C. To explore error profiles and investigate the distinct inductive biases by different distortion types, we used a data-driven approach to group conditions that produce comparable degrees of behavioral deviation. We fitted a Gaussian Mixture Model (GMM) to the distribution of OOD scores across all distortion types and levels (including the undistorted sets), which consistently gave a four-component solution (Bayesian Information Criterion (BIC) and Akaike Information Criterion (AICc); Figure S8 in Appendix. A).

We interpret these groups as qualitatively different regimes of perceptual difficulty (Figure 2.D). We label these groups as reference, near-OOD, far-OOD, and extreme-OOD, ordered by group means. Notably, the conditions that fall within the extreme-OOD level correspond precisely to those yielding chance level human performance, suggesting little or no recognisable information and are potentially of less interest than the other OOD regimes.

## 2.2 Alignment in Human Perceptual Failures

Although the spectrum is constructed based on accuracy, accuracy alone only provides one aspect of behavior – it indicates the degree of recognition failure, but not *how* it fails. Two distortions can yield similar accuracy effect sizes yet produce very different behavioral patterns; participants may show similar accuracy with highly similar error profiles or with entirely different errors. To capture this dimension, we examine human–human error alignment, quantifying how consistently participants misclassify the same images or choose the same incorrect labels. Specifically, we use two complementary metrics: Error Consistency (EC) [13], which measures the overlap of misclassified samples between pairs of participants, and Misclassification Agreement (MA) [14], which measures how often participants predict the same class on samples when both are incorrect.

### 2.2.1 Error alignment across OOD regimes are markedly different

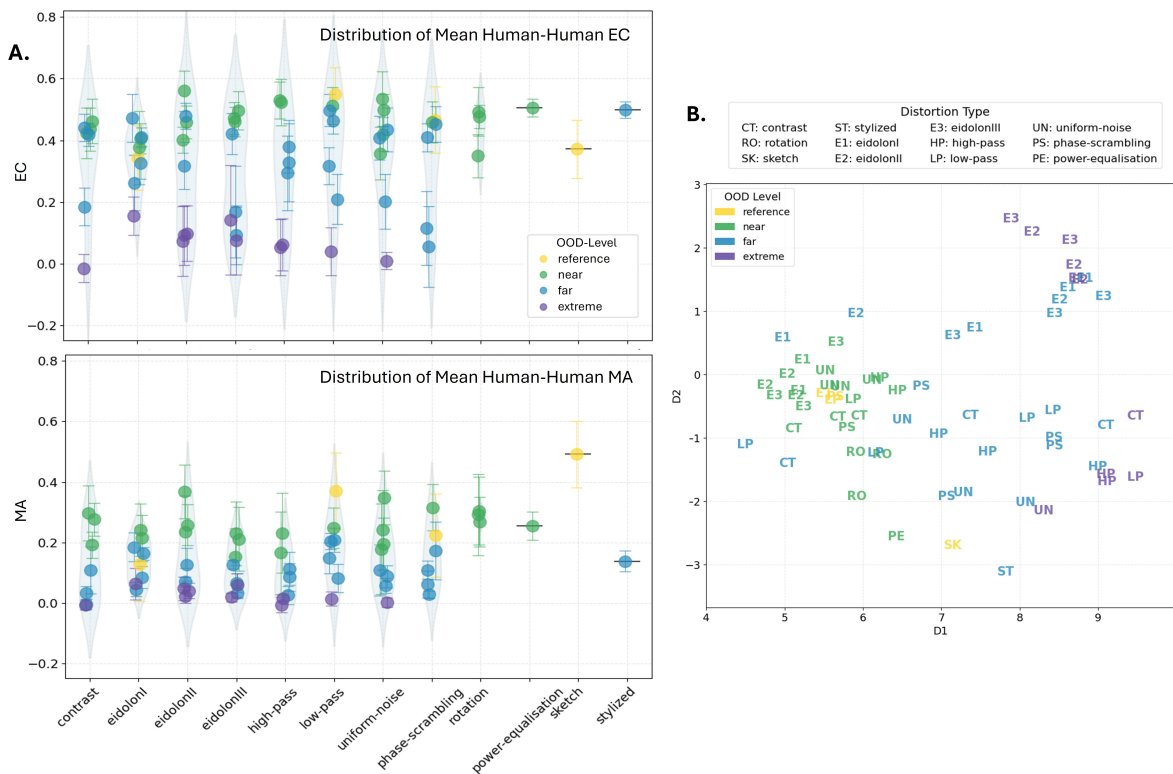


Figure 3: Human-human error alignment A. Dot plots for Error Consistency (EC; top), and Misclassification Agreement (MA; bottom) across distortion types and OOD levels. Each dot represents the mean error alignment value between each pair of participants for a specific level of a distortion, coloured by its OOD category, with vertical bars indicating  $\pm 1$  standard deviation. Transparent violin plots show the distributions of the alignment scores across distortion levels within distortion type. B. t-SNE plot illustrating similarity of human-human error patterns across distortion domains based on the human-human class-level error divergence (CLEED) matrix. Each point represents a distortion condition, labeled by distortion type (e.g., CT: contrast, HP: high-pass). Colors indicate OOD regime they belong to. Spatial proximity reflects similarity in human error patterns across conditions.

We assess human-human error alignment across the four OOD regimes (Figure 3A). We find that extreme-OOD distortions consistently yielded much lower EC values compared to near- and far-OOD conditions, highlighting a pronounced breakdown in shared perceptual strategies under severe distortion (Figure 3A, top). As noted, all conditions in the extreme-OOD region are consistent with chance level accuracies. Distortions also differed in the rate at which EC declines across OOD levels. For instance, *uniform noise* and *phase scrambling* show a sharp drop of EC in the far-OOD regime, whereas distortions such as *high-pass* decrease more gradually, likely reflecting differences in how these manipulations disrupt perceptual features.

Similar to EC, MA declines with increasing perceptual difficulty, with extreme-OOD levels consistently producing the lowest scores (Figure 3A, bottom). In contrast, the difference between far-OOD and extreme-OOD is less pronounced

Do machines fail like humans?

than EC for some distortion types such as *eidolon-I, II* and *high-pass*. The ordering of alignment values across OOD regimes from near to extreme mirrors EC closely, reinforcing the robustness of our perceptual difficulty-based spectrum. The violin plots complement these findings by showing that MA distributions are generally more concentrated than EC distributions and are typically centred at lower values. This indicates that, while participants may often make errors on the same items (captured by EC), it is far less common for them to predict the same incorrect class.

### 2.2.2 Human error profiles are primarily structured by perceptual difficulty (OOD level) rather than distortion type

	Cohens' $D$	Permutation Test	
		$p$ -value	Effect Size
Distortion Type	-0.161	0.025	-2.331
OOD-Level	-0.599	0.000	-12.555

Table 1: Comparison of distortion type and OOD level effects on class-level error divergence (CLED). Reported are Cohen’s  $D$  and permutation test results. Negative  $D$  indicates lower within-group CLED (greater error similarity). OOD level shows a markedly stronger effect than distortion type in both measures.

To further assess whether different severity levels within the same distortion type should be treated as distinct OOD conditions, we compare human error profiles across each OOD level using CLED [14]. Similar to MA, CLED measures the similarity in error patterns between two sets of behavioral responses, but with key differences. As it is a dissimilarity measure, larger values suggest greater difference. More importantly, CLED compares responses at the class level using modified confusion matrices, meaning that there is no requirement for the two response sets to contain the same stimuli, allowing us to directly compare how error profiles vary not only within a distortion type but also across different types and OOD levels.

Previous studies have often treated each distortion type (e.g., *uniform noise* or *low-pass filtering*) as a monolithic condition. Nonetheless, distortions that differ in visual form can impose comparable perceptual challenges and elicit similar error profiles. To capture these relationships, we define each domain as a specific distortion type at a given severity level and construct a CLED-based distance matrix across all domains. This analysis allows us to assess the relative contributions of distortion type and OOD severity to the structure of human error behavior.

The similarity of error profiles across human participants is visualized using t-SNE (Figure 3B). If different severity levels within a distortion type produced similar error profiles, we would expect tight, coherent clusters for each distortion type – conditions of the same type would group together regardless of severity. However, this is not the case: lower and higher severity levels within the same distortion type can be far apart, while conditions from different distortion types sometimes appear more closely aligned. Notably, conditions within the near-OOD regime (green labels) cluster tightly together, whereas their counterparts in far- (blue) or extreme-(purple) OOD regimes are typically more dispersed.

We confirm this through quantitative analyses comparing the effect of distortion type and level. We estimate the separability of within- versus between-group CLED values for distortion-type-based grouping and OOD-level-based grouping using Cohen’s  $D$  and performed permutation tests for statistical inference. The negative values indicate that error patterns of samples within a group (e.g., an OOD level or a distortion type) are more internally consistent than between groups (Table 1). Across both measures, OOD level consistently exhibited a much stronger effect than distortion type, reinforcing that perceptual difficulty is a crucial factor structuring human error profiles.

## 2.3 Model Error Profiles Across the OOD Spectrum: The Role of Distortion Type, Level, and Model Architecture

Human behavior provides a foundation for model–human comparison: the degree of human–human alignment establishes an empirical upper bound on the alignment a model can achieve. Here, we examine model–human alignment across OOD regimes and which architectures show more human-like error patterns.

### 2.3.1 Patterns and variability in model–human alignment across OOD levels

To examine how alignment changes over distortion severity and OOD levels, we plot and describe accuracy, EC, and MA patterns across the full range of distortion levels for three distortion types (Figure 4, *High-Pass*, *Low-Pass* and

## Do machines fail like humans?

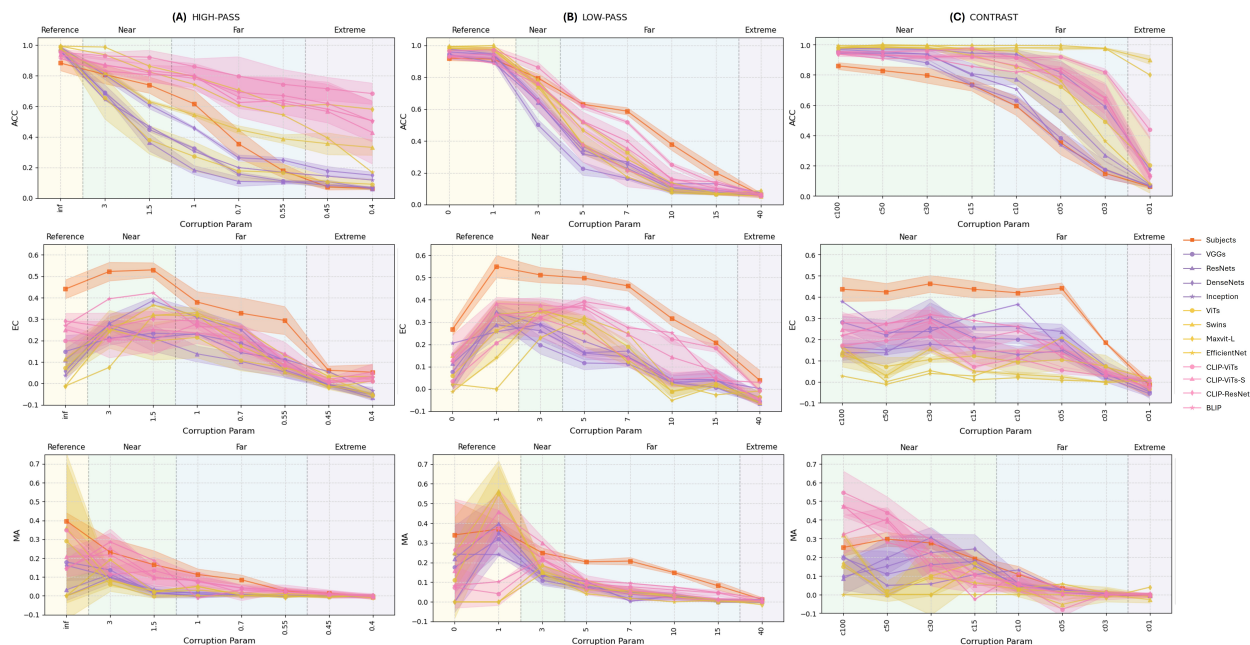


Figure 4: Model-human alignment across distortion levels. Accuracy (ACC, top row), Error Consistency (EC, middle row), and Misclassification Agreement (MA, bottom row) for humans and models across three representative distortion types: High-pass (left), Low-pass (middle), and Contrast (right). Each curve shows the mean: for humans, the mean across participant pairs (orange); for models, the mean across model-human pairs within a subfamily. Curve colours denote superfamilies (CNNs: purple, ViTs: yellow, VLMs: pink), while marker shapes distinguish subfamilies within each superfamily. Shaded regions indicate  $\pm 1$  standard deviation. Curves are plotted against corruption parameters that control the severity, with background shading marking OOD regimes.

*Contrast*; see Figure S9 and S10 for all other distortion types). In general, we observe high variability across OOD levels which suggests analyzing OOD regimes as separate groups.

Accuracy performance and alignment decline as we move from the reference distribution through near- to far-OOD – models broadly track the human trend but differ in where and how they deviate. In the *reference* regime (yellow), models typically exceed human accuracy, though *Contrast* does not have a condition that falls within this region. For some curves, we see an increase in EC in the near OOD region compared to the reference distribution. It is unclear precisely why this is and further investigation may be required. MA is also less informative here due to very few errors. Entering *near-OOD* (green) regime, behavior begins to separate by distortion type. For *High-Pass*, some families keep pace with or exceed human accuracy while others do not. Humans generally outperform most models for *Low-Pass*, whereas most models have higher accuracy than humans for *Contrast*. Across distortion types, human-human EC remains higher than human-model EC. Importantly, EC slightly increases despite reduced accuracy for *High-Pass* and *Contrast*, indicating that people fail on a shared set of samples as perceptual difficulty increases within this regime. MA provides a complementary view: across all distortion types, several models approach human-human MA, meaning that their incorrect predictions resemble human errors. Notably, MA is a stricter criterion than EC, so numerical differences tend to be smaller than in EC.

In the *far-OOD* regime (blue), under *Low-Pass*, humans often outperform models, whereas *High-Pass* and *Contrast* largely preserve their near-OOD ordering. Human-human EC under *High-Pass* becomes more variable (shaded error bars) yet mostly remains above human-model EC. For *Low-Pass*, human-human EC stays higher, though its margin over human-model EC can narrow. Of note, EC for humans for *Contrast* is exceptionally high (see level C05), reflecting strong agreement about some images even at higher distortion levels. MA under *Contrast* is comparatively low, meaning that both humans and models may agree on the correct-incorrect boundary (high EC) but diverge on their mistakes. By contrast, *Low-Pass* produces the largest gap between human-human and model-human MA.

Although alignment degrades with OOD level, the degree of degradation is strongly model-dependent. VLMs tend to maintain higher MA, ViTs struggle under *Low-Pass*, and ViT-based architectures like Swin and MaxViT show robustness under *High-Pass*. However, these patterns vary across OOD regimes, making it difficult to draw conclusions

Model Family	Families	near-OOD		far-OOD	
		p-value	Effect Size	p-value	Effect Size
All	CNN, ViT, VLM	0.001	3.721	<5e-4	14.923
CNN	VGG, ResNet, DenseNet, Inception*	0.005	3.072	<5e-4	4.593
ViT	ViT (l or b), Swin, MaxVit*, EfficientNet*	0.336	0.424	0.057	2.037
VLM	CLIP-ResNet, CLIP-ViT, CLIP-Vit (small), BLIP*	0.014	2.908	0.005	3.323

Table 2: Results of inter- vs intra-family alignment permutation test for near-OOD and far-OOD. Families marked with an asterisk (\*) contain one model so do not contribute to sub-family differences.

about alignment across the full spectrum. Therefore, we focus on quantifying regime-specific alignment in Section 2.3.2 and 2.3.3.

### 2.3.2 Architectural family effects on human alignment

Based on the qualitative observation on Figure 4 (see also Figure S9, S10), models belonging to the same architectural family tend to exhibit characteristic error-alignment profiles. This motivates a natural question: are models architecturally closer to one another, such as those within the same sub-family (e.g., VGGs, ResNets) or within the same broader super-family (e.g., CNNs, ViTs), also closer in how they align with humans? We formalise *two hypotheses*: *H1*) model-human alignment is more similar within sub-families than within super-families; *H2*) model-human alignment is more similar within super-families than across super-families.

We test these hypotheses using permutation tests on model-human alignment profiles. For each model, we concatenate EC and MA values across all distortion types into a single alignment vector and compute pairwise Euclidean distances between models. For *H1*, we compare within-sub-family distances (e.g., VGG-16 vs. VGG-19) to across-sub-family distances within the same super-family (e.g., VGGs vs. ResNets). For *H2*, we compare within-super-family distances to across-super-family distances. The p-values and the effect size are reported in Table 2. At the super-family level, under both OOD regimes, this effect is statistically robust ( $p < 0.01$ ) and with strong effect sizes, suggesting that broad design principles reliably influence model–human alignment. At the sub-family level, results depends upon architectures and OOD regimes.

In general, far-OOD leads to a stronger effect, indicating greater alignment similarity within a model family. For VLMs, intra-family similarity is significantly higher than inter-family similarity. CNNs strongly reject the null hypothesis in both near- and far-OOD regimes, showing the strongest effect sizes among the three superfamilies. By contrast, ViTs do not exhibit statistically reliable sub-family clustering in either regime, suggesting that architectural variations within the ViT family may give rise to more diverse error patterns.

### 2.3.3 Profiles of model-human error alignment over distortion types

To further examine how architectural families influence model–human alignment across distortion types, we select one representative condition for each distortion type from both near- and far-OOD regimes and visualise their alignment profiles using radar plots (Figure 5). Similarity in the shape of the resulting curves indicates similar error patterns between systems, enabling intuitive comparison across architectures. We focus here on results at the model superfamily level; results for individual subfamilies are shown in Figure S12.

In the near-OOD regime, the human–human EC curve is roughly circular with relatively narrow error bars, indicating similar behavioral agreement across distortion types. In general, VLMs and CNNs present higher EC than ViTs. ViTs only surpass CNNs under *Low-Pass* distortions. For MA, human–human alignment is less stable, showing wider error bars and greater variability across distortion types. Several distortion types yield similar EC but markedly different MA patterns. For instance, *Uniform Noise* and *Low-Pass* produce comparable and high human-human EC, but the former yields much higher MA. Conversely, *EidolonII* produces comparatively low EC but exceptionally high MA for both human–human and human–model pairs, implying the same incorrect decisions are often made for the co-errors. CNNs achieve both high EC and MA under *Uniform Noise*. ViTs, by contrast, exhibit both low EC and MA under *Uniform Noise*. VLMs display particularly strong human alignment (especially MA) under *High-Pass* and *Low-Pass*, albeit with substantial variability. All three superfamilies show similarly strong MA under *Power-Equalisation*.

In the far-OOD regime, human–human EC becomes less uniform across distortion types. The EC for *Contrast* and *Uniform Noise* changes only slightly from near- to far-OOD. In contrast, *High-Pass* and *Low-Pass* produce the largest declines in human–human EC. Among model families, CNNs generally exhibit the lowest EC across distortions, except under *Contrast*, where they remain competitive. Under *Low-Pass* and *Uniform Noise*, CNNs’ EC values approach zero.

## Do machines fail like humans?

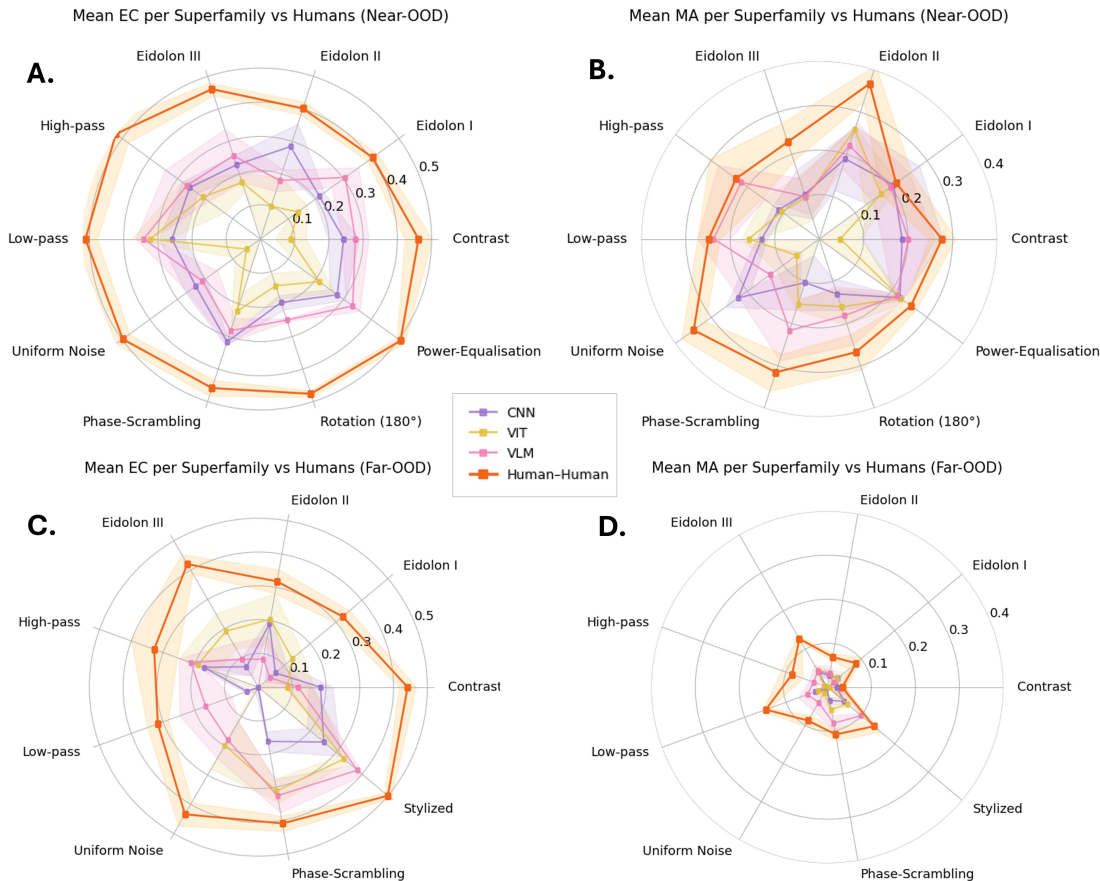


Figure 5: Radar plots of mean model–human error alignment for each superfamily across distortion types, separated by OOD regime (near-OOD, EC (A), MA (B); far-OOD, EC (C), MA (D)). Each axis represents a distortion type, and the radial coordinate indicates model–human alignment scores. Each curve shows the mean EC or MA value for a model superfamily, with error bars indicating  $\pm 1$  standard deviation. Human–human alignment scores are denoted in orange.

ViTs show a distinct advantage in the three *Eidolon* conditions, whereas VLMs achieve exceptionally high EC under *Low-Pass*. For MA, human–human alignment decreases considerably compared with the near-OOD regime, suggesting that under these highly impaired conditions, it becomes much harder for humans to exhibit shared misperceptions. Nonetheless, *Low-Pass*, *Stylized*, and *EidolonIII* maintain comparatively high human–human MA, while *Contrast* leads to minimal agreement on incorrect labels. Across models, VLMs achieve particularly high MA under *Phase-Scrambling* and *Stylized*. ViTs still attain MA values close to those of VLMs in several conditions, although the absolute values remain low. CNNs consistently show very low MA across all distortions.

### 2.3.4 Model-human alignment rankings shifts over OOD regimes reflect different inductive biases

Finally, we examine which models showed the most human-like error patterns by ranking average model-human alignment scores. To compare how models align with humans across different model families, we normalise model–human alignment by human–human alignment. Specifically, for each model  $m$  and condition  $c$ , we compute the alignment ratio

$$\rho_m^c = \frac{a_m^c}{a^c} \quad (2)$$

where  $a_m^c$  is the model’s average alignment with humans (mean value of EC and MA; see Figure S11 for EC and MA separately) and  $a^c$  is the corresponding human–human alignment score for that condition. This ratio accounts for the inherent variability in human agreement under each distortion and evaluate models relative to a human baseline. We note averaging  $\rho_m^c$  over all representative conditions within an OOD regime as  $\bar{\rho}_m$ , a summary statistic for ranking models in that regime. The highest-ranked model in a regime is therefore the one whose alignment with humans is most comparable to the agreement observed among humans themselves.

## Do machines fail like humans?

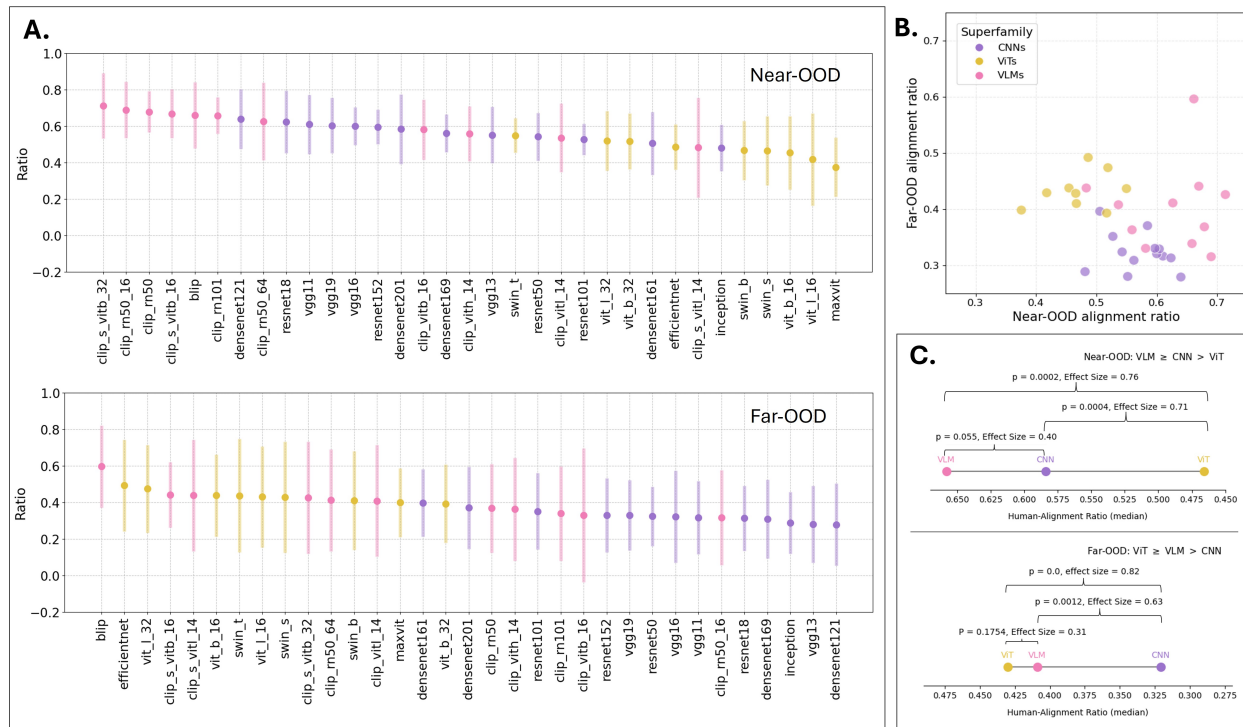


Figure 6: Model–human error alignment rankings. (A) Model–human error alignment values normalised by human–human alignment ordered from most or least aligned in near- (top) and far-OOD (bottom) regimes. Values are the ratio of model–human alignment to human–human alignment, where higher values indicate that the error patterns between those models and humans are closer to the baseline agreement among humans. Each dot represents a model, with vertical bars showing  $\pm 1$  SD confidence interval. Colours denote model families (CNNs in purple, ViTs in yellow, VLMs in pink). (B) Scatter plot of alignment ratio near-OOD (x-axis) and far-OOD (y-axis) conditions. (C) Pairwise statistical ranking of model superfamilies under near- and far-OOD regimes. Each plot summarises Mann–Whitney U tests comparing the ranks between model families; “>” indicates a significant rank advantage ( $p < 0.01$ ), while “ $\geq$ ” denotes a non-significant difference. Median alignment ratios are shown only to aid visual interpretation.

The rankings of  $\bar{\rho}_m$  for the models in near- and far-OOD regimes are shown in Figure 6A and the alignment ratios for each model in near and far-OOD regime are presented in Figure 6B. We find considerable differences in model-human alignment between near- and far-OOD: many models that align closely with humans in near-OOD no longer rank highly in far-OOD, showing that perceptual difficulty reshapes the human-based behavioral consistency of models (Figure 6A). In the near-OOD regime, VLMs and CNNs tend to achieve a higher alignment ratio than ViTs ( $p$ 's  $< 0.01$ ), although ViTs typically outperform CNNs in standard recognition tasks.

In the far-OOD regime, VLMs maintain high alignment rankings, but to a similar level to ViTs, both of which had higher human alignment over CNNs ( $p < 0.01$ ; Figure 6C). If VLMs exhibit greater model-human alignment due to language and semantic knowledge from their text-based training, this suggests that semantic information is marked affected and even completely removed in far-OOD regimes.

## 3 Discussion

Model-human alignment comparisons have typically treated different distortion types and levels similarly, despite being distinct in nature. Our human-centered framework addresses this issue by defining an OOD spectrum that groups conditions by human perceptual difficulty, rather than by arbitrary parameter-based severity levels. We show that model-human alignment depends on the type and level of distortion, where vision-language models are the most consistently human-aligned across both near- and far-OOD conditions, but CNNs are more aligned than ViTs for near OOD and ViTs are more aligned than CNNs for far OOD.

### 3.1 Why a Human-Centred OOD Spectrum

When models are exposed to distributional shifts, the way their performance degrades can reveal their inductive biases – the visual features they exploit for recognition. The error profile across distortion types thus serves as a behavioral signature of a system’s information-processing strategies. However, drawing valid conclusions requires a principled way to compare distortions. Distortion parameters are incommensurable across types, and prior approaches, including aggregating across severity levels, qualitatively selecting comparable distortions, or normalising to a reference model [21, 26, 29], each introduce limitations. Our perceptual OOD spectrum grounded in human perceptual difficulty addresses this by quantifying and grouping conditions by deviation from human performance under standard, baseline performance, rather than deviation from training statistics or arbitrary parameters. The resulting OOD spectrum provides a principled basis for assessing whether models fail like humans across the full spectrum of perceptual challenge.

First, this framework allows meaningful comparisons at matched levels of human perceptual difficulty across distortion types. Without such matching, apparent differences in alignment may simply reflect task difficulty rather than genuine architectural biases. For example, *Eidolon I* parameter 8, *High-Pass* parameter 1, and *Low-Pass* parameter 5 induce similar levels of behavioral shift from baseline, even though they appear visually very different. Second, it enables the identification of appropriate conditions for evaluating model-human alignment. Applying this method reveals four regimes: reference, representing natural variation on undistorted or lightly distorted images; near-OOD, representing moderate accuracy reduction; far-OOD, a transitional zone where performance declines at varying rates across distortion types; and extreme-OOD, where images lack sufficient information for recognition and performance falls to or below chance. Qualitatively speaking, reference, near-OOD, and extreme-OOD emerged as strongly coherent components, while far-OOD is more diffuse, likely due to sparse sampling in this range. When both humans and models fail entirely, alignment values become uninformative. We therefore exclude extreme-OOD for evaluation. Prior work that aggregated extreme-OOD conditions may have led to conclusions that are not well supported under finer-grained OOD analysis.

### 3.2 Establishing the Human–Human Behavioral Alignment Baseline

Human-human alignment patterns across the OOD spectrum strongly suggest that near-OOD and far-OOD regimes should be evaluated separately, as systems likely rely on different strategies across these conditions. In the near-OOD regime, humans show roughly uniform EC across distortions, suggesting that errors may primarily target "harder" undistorted images – those that become ambiguous under minor degradation. Such errors depend more on the stimulus than the observer. Human–human MA is also relatively high for near-OOD, meaning distortions which obscure the true class are also likely to suggest a *specific* alternative, a "false lead" that consistently draws multiple observers toward the same incorrect response, reflecting strong stimulus-driven effects.

In the far-OOD regime, this pattern shifts. EC degrades gracefully, indicating that individual differences in responses increases as distortions become more severe, reflecting observer dependence rather than purely stimulus effects. MA degrades more quickly than EC, suggesting that while false leads are still present, they become less common. This suggests that stronger distortions disrupt recognition in different ways from system to system. At extreme-OOD, both metrics flatline, implying no meaningful class information remains. MA in particular indicates that false leads are almost entirely absent. The absence of both accurate predictions and systematic error biases reflects a lack of meaningful human–human alignment in this regime where human–model alignment cannot be meaningfully assessed. Researchers should therefore avoid these conditions when drawing conclusions.

These regime-specific patterns can be understood in terms of how EC and MA relate to stimulus space. EC and MA inform us about the alignment between two systems’ decision boundaries in stimulus space – the degree to which two systems agree, but they are sensitive to the data distribution on which they are computed [13, 14]. As different distortion levels produce distinct data distributions occupying different regions of stimulus space, computing EC and MA across pooled distortion levels would conflate alignment patterns that may differ substantially across these regions. Our findings support this concern: EC and MA vary considerably across distortion levels within the same distortion type, demonstrating that pooling across severity levels would obscure meaningful variation in alignment.

EC and MA reveal how humans align within a given distortion condition, but not whether error patterns are similar across conditions. CLED addresses this by comparing behavioral responses across non-overlapping stimulus sets. The implication is that distortion conditions with low CLED impair the visual features to which humans are sensitive in similar ways. This can arise by chance due to the sparsity of errors when both conditions are easy (high accuracy). If they are both hard and CLED is low, the relevant visual features upon which humans depend to make decisions may have been impaired in similar ways. If one condition is easy and another hard, then the hard distortion would need to somehow balance the impairment evenly across the visual features used for classification to produce a similar error pattern. This seems less plausible, and we would therefore expect distortions of different levels of difficulty to typically

Do machines fail like humans?

have higher CLEDs than pairs of similar difficulty. Both the t-SNE visualisation and quantitative analysis confirm this: OOD level exerts a stronger effect on human error structure than distortion type.

Taken together, these findings suggest that humans employ different decision-making strategies at different levels of perceptual difficulty: in near-OOD, errors are stimulus-driven and consistent across observers, while in far-OOD, errors become more observer-dependent and less systematic. To explore whether models align with humans in their information-processing strategies, we must therefore evaluate these regimes separately – a model that aligns with human errors in near-OOD may not do so in far-OOD, and vice versa.

### 3.3 Trajectories of Alignment: Models versus humans

The trajectories of model accuracy and model–human alignment across distortion levels (Figure 4) reveal that different distortion types elicit markedly different responses from models, both in terms of accuracy and alignment with human behavior. These divergences in accuracy and alignment profiles indicate that models exploit different visual features from humans for these classification tasks. When a model is more sensitive than humans to a particular distortion, it suggests the model relies more heavily on features that this distortion selectively disrupts. Conversely, when a model is more resilient than humans, it may exploit features that humans either do not use or weight less heavily.

Several patterns emerge from the trajectories. First, human accuracy is more stable across distortion types than model accuracy – models show greater variability in how different distortions impair their performance. Second, human–human EC consistently exceeds model–human EC for almost all models, and human–human MA, in some cases, is substantially higher than model–human MA. This indicates that humans share more similar visual features for classification with each other than with models: whether one participant misclassifies a distorted image is more predictive of another participant’s response than of any model’s response. In short, the visual features humans rely on overlap more with each other than with those exploited by models.

### 3.4 Alignment fingerprints across model families

As noted above, humans show roughly uniform EC with other humans for all near-OOD distortions, but model–human EC is substantially lower even for these mild distortions. This indicates that models are impaired by distortions in ways that humans are not. Moreover, different model families appear to be impaired differently by various distortions, suggesting that certain families rely on visual features that others do not, or weigh differently. Human–human MA is also relatively high for near-OOD distortions, and though lower, model–human MA remains moderately high. This implies that some false leads for humans are the same false leads for models too, particularly for certain distortion types such as *power equalisation*. In the far-OOD regime, EC and MA are reduced more sharply for some distortion types than others, and these patterns also differ across model families.

The radar plot (Figure 5) shows that the profile of model–human alignment across distortion types serves as a characteristic fingerprint of each model family. This fingerprint captures how a given architecture responds to different forms of image degradation relative to human perception. Our quantitative analysis reinforces this interpretation. Models are more alike within superfamilies than between superfamilies, and more alike within superfamilies than with other models in the same superfamily, although whether this reflects purely architectural effects or whether training also plays a role remains unclear. We interpret these fingerprints as evidence that model families differ in the visual features they exploit, and hence in their sensitivity to distortions that impair those features.

### 3.5 Model-human alignment rankings shift across the OOD spectrum

We find that VLMs were most consistently aligned with human behavior across the spectrum, CNNs were more aligned than ViTs for near-OOD, and ViTs were comparable to VLMs and better than CNNs for far-OOD regimes. These regime-dependent patterns reveal how architectural biases manifest differently under varying levels of degradation. CNNs achieve high near-OOD alignment despite their texture bias [15], which may reflect two possibilities. First, when texture and shape cues remain partially intact in near-OOD, CNNs align with humans while relying on fundamentally different features – texture and shape are often correlated in images, allowing different strategies to converge on similar outputs. Second, under moderate degradation, humans may draw on multiple features rather than relying on shape alone such as exploiting informative texture cues, thereby aligning more with CNNs. CNNs’ behavior in far-OOD catastrophically diverges from humans, with EC and MA approaching zero. This reveals that the representations CNNs develop do not align with human behavior when information becomes severely degraded, and that high alignment in normal to mildly degraded conditions does not guarantee alignment in general.

ViTs uniquely demonstrate the poorest near-OOD alignment with humans despite often maintaining high or even superior accuracy compared to other architectures. This means that high accuracy does not necessarily translate to

Do machines fail like humans?

human-like error patterns – ViTs can achieve strong overall performance whilst making different errors to humans. In contrast, ViTs achieve the strongest alignment in the far-OOD regime, comparable to VLMs. Under severe degradation, ViTs maintain behavioral correspondence with humans compared to CNNs. Indeed, ViTs are less texture-dependent than CNNs [35] which may contribute to their sustained far-OOD alignment: when severe distortions remove fine details, ViTs’ reduced reliance on high-frequency texture features may allow them to make human-like decisions based on remaining coarse information.

VLMs demonstrate sustained strong alignment across both regimes. Notably, VLMs with CNN-based visual encoders show higher alignment in near-OOD than far-OOD, reflecting architectural biases inherited from the visual backbone. BLIP’s exceptional cross-regime stability may reflect its training approach: bootstrapping with synthetic captions may result in more robust semantic representations that generalise across degradation levels. VLMs language-based semantic knowledge may guide its behavior toward human-like decisions, especially in near-OOD. However, for far-OOD conditions, visual information may have degraded to the extent that semantic information is no longer available, leading to similar human alignment levels to the image only version of their model backbone. Language-grounded representations may guide VLMs toward human-like confusion patterns. This parallels how human semantic knowledge constrains perceptual interpretation under uncertainty [36, 37], suggesting that multimodal training provides semantic scaffolding that remains accessible even when low-level visual features become unreliable.

Despite strong and consistent alignment in some models, human–human alignment remains a ceiling that no model approaches. This tells us that information processing in the human visual system and current AI models is still significantly different. This gap matters for two reasons. First, human vision exhibits graceful degradation across distortion types – not necessarily achieving high accuracy, but maintaining consistent, slowly degrading performance rather than unpredictably excelling on some while catastrophically failing on other distortions. Models that align with human error patterns are likely exploiting features that support this stability, whereas models that diverge may rely on features that are brittle. Second, human alignment relates to trustworthiness. A model that makes human-like errors in human-like ways is more predictable and interpretable in deployment. Such failures are more acceptable because they mirror the limitations of human perception rather than reflecting opaque, non-intuitive biases. Our framework provides a tool to quantify both dimensions, measuring whether future architectures might achieve not just high accuracy, but human-like robustness and trustworthy behavior.

### 3.6 Future Work

Future research could conduct larger-scale human studies with denser parameter sampling across distortion severity levels would strengthen conclusions about regime boundaries, better characterise the far-OOD transitional regime, and provide more reliable estimates of human–human baseline alignment. Second, our spectrum is constructed from synthetic corruptions; extending this framework to natural distributional shifts would test generalisability. Third, we focus on object recognition with static images; extending to domains such as scene understanding or video would test whether the architectural biases we observe are domain-general.

## 4 Materials and Methods

### 4.1 Dataset

We used the *modelvshuman* benchmark [22], which provides images from 16 object categories with human behavioral data collected under controlled laboratory conditions. Images are systematically distorted across multiple severity levels to probe robustness under OOD conditions. From the 17 available distortion types, we used 14 subsets spanning diverse distortion families including uniform noise, high-pass, low-pass, contrast, phase noise, and Eidolon variants.

### 4.2 Tested Models

We evaluated 31 models spanning three architectural families: CNNs, ViTs, and VLMs. CNNs included VGG variants (VGG-11, -13, -16, -19) [34], ResNet variants (ResNet-18, -50, -101, -152) [38], DenseNet variants (DenseNet-121, -161, -169, -201) [39], Inception-v3 [40], and EfficientNet [41]. ViTs included four vanilla ViT variants [33], three Swin Transformers [42], and MaxViT-L [43]. All CNNs and most ViTs were pretrained on ImageNet-1K; EfficientNet was pretrained on a larger dataset. For VLMs, we tested BLIP [44], CLIP-ViT variants trained on DFN-2B, CLIP-ViT variants trained by OpenAI, and CLIP-ResNet variants trained by OpenAI [32]. Model details are presented in the supplementary materials.\*

---

\*[https://docs.google.com/spreadsheets/d/1ldqG8L1Qd\\_tDh9f3xdZQRA3v2UffUIhaLds2wTrhoLU/edit?usp=sharing](https://docs.google.com/spreadsheets/d/1ldqG8L1Qd_tDh9f3xdZQRA3v2UffUIhaLds2wTrhoLU/edit?usp=sharing)

### 4.3 Error Alignment Metrics

We employed three complementary metrics to characterise model–human behavior under distribution shift. Error consistency (EC) [13] and misclassification agreement (MA) [14] were used to quantify model–human error alignment under matched visual conditions, while class-level error divergence (CLED) [14] was used to measure differences in error structure across OOD conditions. All metrics were computed separately for each distortion type and severity level using model predictions and human responses on the same image set.

EC measures the degree to which two systems produce correct or incorrect responses on the same stimuli. Formally, EC is defined as Cohen’s  $K$  computed over binary correctness outcomes, comparing the observed agreement in correctness to the agreement expected by chance given the marginal accuracies of the two systems. MA quantifies alignment in how errors are made when both systems misclassify the same stimuli. MA is computed by restricting the analysis to jointly misclassified instances and measuring agreement between the predicted class labels of the two systems using a multiclass Cohen’s  $K$  statistic. CLED is computed by comparing class-wise error distributions derived from confusion matrices restricted to error instances, using a weighted Jensen–Shannon divergence across classes.

## References

- [1] Nikolaus Kriegeskorte. Deep neural networks: a new framework for modeling biological vision and brain information processing. *Annual review of vision science*, 1(1):417–446, 2015.
- [2] Radoslaw M Cichy and Daniel Kaiser. Deep neural networks as scientific models. *Trends in cognitive sciences*, 23(4):305–317, 2019.
- [3] Friedemann Pulvermüller, Rosario Tomasello, Malte R Henningsen-Schomers, and Thomas Wennekers. Biological constraints on neural network models of cognitive function. *Nature Reviews Neuroscience*, 22(8):488–502, 2021.
- [4] Rishi Rajalingham, Elias B Issa, Pouya Bashivan, Kohitij Kar, Kailyn Schmidt, and James J DiCarlo. Large-scale, high-resolution comparison of the core visual object recognition behavior of humans, monkeys, and state-of-the-art deep artificial neural networks. *Journal of Neuroscience*, 38(33):7255–7269, 2018.
- [5] Iliia Sucholutsky, Lukas Muttenthaler, Adrian Weller, Andi Peng, Andreea Bobu, Been Kim, Bradley C Love, Erin Grant, Iris Groen, Jascha Achterberg, et al. Getting aligned on representational alignment. *arXiv preprint arXiv:2310.13018*, 2023.
- [6] Joshua C Peterson, Ruairidh M Battleday, Thomas L Griffiths, and Olga Russakovsky. Human uncertainty makes classification more robust. In *Proceedings of the IEEE/CVF international conference on computer vision*, pages 9617–9626, 2019.
- [7] Lukas Muttenthaler, Klaus Greff, Frieda Born, Bernhard Spitzer, Simon Kornblith, Michael C Mozer, Klaus-Robert Müller, Thomas Unterthiner, and Andrew K Lampinen. Aligning machine and human visual representations across abstraction levels. *Nature*, 647(8089):349–355, 2025.
- [8] Thomas Fel, Ivan F Rodriguez Rodriguez, Drew Linsley, and Thomas Serre. Harmonizing the object recognition strategies of deep neural networks with humans. *Advances in neural information processing systems*, 35:9432–9446, 2022.
- [9] Aidan Boyd, Mohamed Trabelsi, Huseyin Uzunalioglu, and Dan Kushnir. Increasing interpretability of neural networks by approximating human visual saliency. *arXiv preprint arXiv:2410.16115*, 2024.
- [10] Drew Linsley, Pinyuan Feng, Thibaut Boissin, Alekh Karkada Ashok, Thomas Fel, Stephanie Olaiya, and Thomas Serre. Adversarial alignment: Breaking the trade-off between the strength of an attack and its relevance to human perception. *arXiv preprint arXiv:2306.03229*, 2023.
- [11] Blaine Hoak, Kunyang Li, and Patrick McDaniel. Alignment and adversarial robustness: Are more human-like models more secure? *arXiv preprint arXiv:2502.12377*, 2025.
- [12] Ali Borji and Laurent Itti. Human vs. computer in scene and object recognition. In *Proceedings of the IEEE conference on computer vision and pattern recognition*, pages 113–120, 2014.
- [13] Robert Geirhos, Kristof Meding, and Felix A. Wichmann. Beyond accuracy: quantifying trial-by-trial behaviour of cnns and humans by measuring error consistency. In *Proceedings of the 34th International Conference on Neural Information Processing Systems, NIPS ’20*, Red Hook, NY, USA, 2020. Curran Associates Inc.
- [14] Binxia Xu, Antonis Bikakis, Daniel FO Onah, Andreas Vlachidis, and Luke Dickens. Measuring error alignment for decision-making systems. In *Proceedings of the AAAI Conference on Artificial Intelligence*, volume 39, pages 27731–27739, 2025.

- [15] Robert Geirhos, Patricia Rubisch, Claudio Michaelis, Matthias Bethge, Felix A Wichmann, and Wieland Brendel. Imagenet-trained cnns are biased towards texture; increasing shape bias improves accuracy and robustness. In *International conference on learning representations*, 2018.
- [16] Nicholas Baker, Hongjing Lu, Gennady Erlikhman, and Philip J Kellman. Deep convolutional networks do not classify based on global object shape. *PLoS computational biology*, 14(12):e1006613, 2018.
- [17] Colin Conwell, Jacob S Prince, Kendrick N Kay, George A Alvarez, and Talia Konkle. A large-scale examination of inductive biases shaping high-level visual representation in brains and machines. *Nature communications*, 15(1):9383, 2024.
- [18] Saeed R Kheradpisheh, Masoud Ghodrati, Mohammad Ganjtabesh, and Timothée Masquelier. Humans and deep networks largely agree on which kinds of variation make object recognition harder. *Frontiers in computational neuroscience*, 10:92, 2016.
- [19] Samuel Dodge and Lina Karam. A study and comparison of human and deep learning recognition performance under visual distortions. In *2017 26th international conference on computer communication and networks (ICCCN)*, pages 1–7. IEEE, 2017.
- [20] Robert Geirhos, Carlos RM Temme, Jonas Rauber, Heiko H Schütt, Matthias Bethge, and Felix A Wichmann. Generalisation in humans and deep neural networks. *Advances in neural information processing systems*, 31, 2018.
- [21] Dan Hendrycks and Thomas Dietterich. Benchmarking neural network robustness to common corruptions and perturbations. *Proceedings of the International Conference on Learning Representations*, 2019.
- [22] Robert Geirhos, Kantharaju Narayanappa, Benjamin Mitzkus, Tizian Thieringer, Matthias Bethge, Felix A Wichmann, and Wieland Brendel. Partial success in closing the gap between human and machine vision. In *Advances in Neural Information Processing Systems 34*, 2021.
- [23] Sebastian Farquhar and Yarin Gal. What ‘out-of-distribution’ is and is not. In *Neurips ml safety workshop*, 2022.
- [24] Dan Hendrycks and Kevin Gimpel. A baseline for detecting misclassified and out-of-distribution examples in neural networks. *arXiv preprint arXiv:1610.02136*, 2016.
- [25] Rohan Taori, Achal Dave, Vaishaal Shankar, Nicholas Carlini, Benjamin Recht, and Ludwig Schmidt. Measuring robustness to natural distribution shifts in image classification. *Advances in Neural Information Processing Systems*, 33:18583–18599, 2020.
- [26] Samuel Dodge and Lina Karam. Understanding how image quality affects deep neural networks. In *2016 eighth international conference on quality of multimedia experience (QoMEX)*, pages 1–6. IEEE, 2016.
- [27] Felix A Wichmann, David HJ Janssen, Robert Geirhos, Guillermo Aguilar, Heiko H Schütt, Marianne Maertens, and Matthias Bethge. Methods and measurements to compare men against machines. *Electronic Imaging*, 29:36–45, 2017.
- [28] Girik Malik, Dakarai Crowder, and Ennio Mingolla. Extreme image transformations affect humans and machines differently. *Biological Cybernetics*, 117(4):331–343, 2023.
- [29] Alex Krizhevsky, Ilya Sutskever, and Geoffrey E Hinton. Imagenet classification with deep convolutional neural networks. *Advances in neural information processing systems*, 25, 2012.
- [30] Larry V Hedges. Distribution theory for glass’s estimator of effect size and related estimators. *journal of Educational Statistics*, 6(2):107–128, 1981.
- [31] Vishwakumara Kayargadde and Jean-Bernard Martens. Perceptual characterization of images degraded by blur and noise: model. *Journal of the Optical Society of America A*, 13(6):1178–1188, 1996.
- [32] Alec Radford, Jong Wook Kim, Chris Hallacy, Aditya Ramesh, Gabriel Goh, Sandhini Agarwal, Girish Sastry, Amanda Askell, Pamela Mishkin, Jack Clark, et al. Learning transferable visual models from natural language supervision. In *International conference on machine learning*, pages 8748–8763. PmLR, 2021.
- [33] Alexey Dosovitskiy. An image is worth 16x16 words: Transformers for image recognition at scale. *arXiv preprint arXiv:2010.11929*, 2020.
- [34] Karen Simonyan and Andrew Zisserman. Very deep convolutional networks for large-scale image recognition. *arXiv preprint arXiv:1409.1556*, 2014.
- [35] Shikhar Tuli, Ishita Dasgupta, Erin Grant, and Thomas L Griffiths. Are convolutional neural networks or transformers more like human vision? *arXiv preprint arXiv:2105.07197*, 2021.
- [36] Gary Lupyan and Emily J Ward. Language can boost otherwise unseen objects into visual awareness. *Proceedings of the National Academy of Sciences*, 110(35):14196–14201, 2013.

- [37] Peter D Weller, Milena Rabovsky, and Rasha Abdel Rahman. Semantic knowledge enhances conscious awareness of visual objects. *Journal of Cognitive Neuroscience*, 31(8):1216–1226, 2019.
- [38] Kaiming He, Xiangyu Zhang, Shaoqing Ren, and Jian Sun. Deep residual learning for image recognition. In *Proceedings of the IEEE conference on computer vision and pattern recognition*, pages 770–778, 2016.
- [39] Gao Huang, Zhuang Liu, Laurens Van Der Maaten, and Kilian Q Weinberger. Densely connected convolutional networks. In *Proceedings of the IEEE conference on computer vision and pattern recognition*, pages 4700–4708, 2017.
- [40] Christian Szegedy, Vincent Vanhoucke, Sergey Ioffe, Jon Shlens, and Zbigniew Wojna. Rethinking the inception architecture for computer vision. In *Proceedings of the IEEE conference on computer vision and pattern recognition*, pages 2818–2826, 2016.
- [41] Mingxing Tan and Quoc Le. Efficientnet: Rethinking model scaling for convolutional neural networks. In *International conference on machine learning*, pages 6105–6114. PMLR, 2019.
- [42] Ze Liu, Yutong Lin, Yue Cao, Han Hu, Yixuan Wei, Zheng Zhang, Stephen Lin, and Baining Guo. Swin transformer: Hierarchical vision transformer using shifted windows. In *Proceedings of the IEEE/CVF international conference on computer vision*, pages 10012–10022, 2021.
- [43] Zhengzhong Tu, Hossein Talebi, Han Zhang, Feng Yang, Peyman Milanfar, Alan Bovik, and Yinxiao Li. Maxvit: Multi-axis vision transformer. In *European conference on computer vision*, pages 459–479. Springer, 2022.
- [44] Junnan Li, Dongxu Li, Caiming Xiong, and Steven Hoi. Blip: Bootstrapping language-image pre-training for unified vision-language understanding and generation. In *International conference on machine learning*, pages 12888–12900. PMLR, 2022.

## Appendix

Code is available at <https://github.com/xubinxia/ood-spectrum>.

### A. Statistical Evidence for the Construction of OOD Spectrum

(a) Part I			(b) Part II		
Distortion	raw $p$	adjusted $p$	Distortion	raw $p$	adjusted $p$
<b>contrast_c100</b>	-	-	<b>high-pass_inf</b>	-	-
contrast_c50	0.00731	0.00835	high-pass_3	0.00565	0.00680
contrast_c30	0.00565	0.00680	high-pass_1.5	0.00154	0.00250
contrast_c15	0.00170	0.00257	high-pass_1	0.00154	0.00250
contrast_c10	0.00154	0.00250	high-pass_0.7	0.00154	0.00250
contrast_c05	0.00154	0.00250	high-pass_0.55	0.00154	0.00250
contrast_c03	0.00154	0.00250	high-pass_0.45	0.00154	0.00250
contrast_c01	0.00154	0.00250	high-pass_0.4	0.00154	0.00250
<b>rotation_0</b>	-	-	<b>low-pass_0</b>	-	-
rotation_90	0.01414*	0.01532*	low-pass_1	0.13754*	0.13972*
rotation_180	0.00274	0.00356	low-pass_3	0.00249	0.00330
rotation_270	0.01531*	0.01605*	low-pass_5	0.00154	0.00250
eidolonI_1-10-10	0.00867	0.00971	low-pass_7	0.00154	0.00250
eidolonI_2-10-10	0.75350*	0.75350*	low-pass_10	0.00154	0.00250
eidolonI_4-10-10	0.01023*	0.01127*	low-pass_15	0.00154	0.00250
eidolonI_8-10-10	0.00187	0.00271	low-pass_40	0.00154	0.00250
eidolonI_16-10-10	0.00154	0.00250	uniform-noise_0.00	0.00206	0.00291
eidolonI_32-10-10	0.00154	0.00250	uniform-noise_0.03	0.00730	0.00835
eidolonI_64-10-10	0.00154	0.00250	uniform-noise_0.05	0.00170	0.00257
eidolonI_128-10-10	0.00154	0.00250	uniform-noise_0.10	0.00187	0.00271
eidolonII_1-3-10	0.00433	0.00541	uniform-noise_0.20	0.00154	0.00250
eidolonII_2-3-10	0.00170	0.00257	uniform-noise_0.35	0.00154	0.00250
eidolonII_4-3-10	0.00249	0.00330	uniform-noise_0.60	0.00154	0.00250
eidolonII_8-3-10	0.00154	0.00250	uniform-noise_0.90	0.00154	0.00250
eidolonII_16-3-10	0.00154	0.00250	<b>phase-scrambling_0</b>	-	-
eidolonII_32-3-10	0.00154	0.00250	phase-scrambling_30	0.13757*	0.13972*
eidolonII_64-3-10	0.00154	0.00250	phase-scrambling_60	0.00226	0.00313
eidolonII_128-3-10	0.00154	0.00250	phase-scrambling_90	0.00154	0.00250
eidolonIII_1-0-10	0.00732	0.00835	phase-scrambling_120	0.00154	0.00250
eidolonIII_2-0-10	0.00329	0.00420	phase-scrambling_150	0.00154	0.00250
eidolonIII_4-0-10	0.00154	0.00250	phase-scrambling_180	0.00154	0.00250
eidolonIII_8-0-10	0.00154	0.00250	<b>power-equalisation_0</b>	-	-
eidolonIII_16-0-10	0.00154	0.00250	power-equalisation_pow	0.00154	0.00250
eidolonIII_32-0-10	0.00154	0.00250	<b>colour_bw</b>	-	-
eidolonIII_64-0-10	0.00154	0.00250	sketch	0.01486*	0.01583*
eidolonIII_128-0-10	0.00154	0.00250	stylized	0.00048	0.00250

Table 2: Mann–Whitney U test  $p$ -values (raw and BH-corrected) for all distortion conditions. Each  $p$ -value indicates whether the distribution of human accuracies under the distortion differs significantly from the non-distorted baseline. Lower values (e.g.,  $p < 0.01$ ) suggest a statistically significant shift in prediction behavior. The adjusted  $p$  values (corrected by the Benjamini–Hochberg procedure) are used to reject conditions under false discovery rate control at  $\alpha = 0.01$ . Bold rows denote conditions with no distortion applied (reference condition/baseline). Asterisks (\*) mark conditions with raw  $p > 0.01$  (all of them also rejected the null hypothesis after the BH-procedure).

(a) Part I			(b) Part II		
Distortion	adjusted $p$	reject $H_0$	Distortion	adjusted $p$	reject $H_0$
contrast_c50	0	True	high-pass_3	0	True
contrast_c30	0	True	high-pass_1.5	0	True
contrast_c15	0	True	high-pass_1	1.9e-299	True
contrast_c10	4.6e-283	True	high-pass_0.7	3.9e-106	True
contrast_c05	3.9e-106	True	high-pass_0.55	4.1e-24	True
contrast_c03	1.5e-15	True	high-pass_0.45	0.13	<b>False</b>
contrast_c01	0.47	<b>False</b>	high-pass_0.4	0.41	<b>False</b>
rotation_90	0	True	low-pass_1	0	True
rotation_180	0	True	low-pass_3	0	True
rotation_270	0	True	low-pass_5	5.4e-312	True
eidolonI_1-10-10	0	True	low-pass_7	5e-275	True
eidolonI_2-10-10	0	True	low-pass_10	4.3e-123	True
eidolonI_4-10-10	0	True	low-pass_15	8.1e-32	True
eidolonI_8-10-10	0	True	low-pass_40	0.52	<b>False</b>
eidolonI_16-10-10	6.4e-162	True	uniform-noise_0.00	0	True
eidolonI_32-10-10	2.4e-40	True	uniform-noise_0.03	0	True
eidolonI_64-10-10	5.6e-09	True	uniform-noise_0.05	0	True
eidolonI_128-10-10	0.074	<b>False</b>	uniform-noise_0.10	0	True
eidolonII_1-3-10	0	True	uniform-noise_0.20	0	True
eidolonII_2-3-10	0	True	uniform-noise_0.35	6.6e-134	True
eidolonII_4-3-10	0	True	uniform-noise_0.60	4.1e-15	True
eidolonII_8-3-10	8.6e-253	True	uniform-noise_0.90	0.098	<b>False</b>
eidolonII_16-3-10	1.4e-43	True	phase-scrambling_30	0	True
eidolonII_32-3-10	0.04	<b>False</b>	phase-scrambling_60	0	True
eidolonII_64-3-10	0.2	<b>False</b>	phase-scrambling_90	0	True
eidolonII_128-3-10	0.24	<b>False</b>	phase-scrambling_120	6e-129	True
eidolonIII_1-0-10	0	True	phase-scrambling_150	6.4e-06	True
eidolonIII_2-0-10	0	True	phase-scrambling_180	6.9e-05	True
eidolonIII_4-0-10	0	True	power-equalisation_pow	0	True
eidolonIII_8-0-10	6.2e-139	True	sketch	0	True
eidolonIII_16-0-10	2.1e-16	True	stylized	0	True
eidolonIII_32-0-10	2.2e-05	True			
eidolonIII_64-0-10	0.2	<b>False</b>			
eidolonIII_128-0-10	0.52	<b>False</b>			

Table 3: Results of binomial tests under the null hypothesis  $P(1/16)$ .

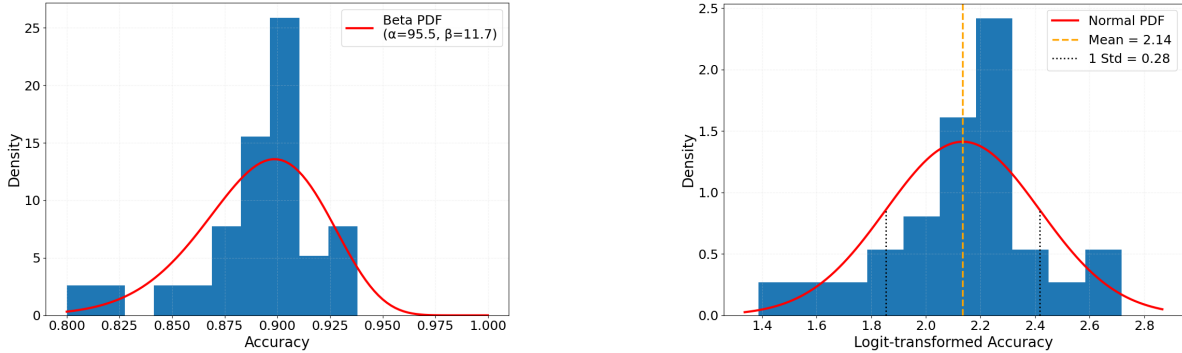
## Do machines fail like humans?

To assess whether human accuracy scores were normally distributed, we first plot the probability density of the 28 accuracy values in Figure 7a. As shown, the accuracy scores are very close to 1. Due to this upper bound, the distribution is left-skewed, which is not ideal for parametric tests that assume normality and symmetric variance. To deal with this issue, we apply the logit transformation:

$$\text{logit}(a) = \ln\left(\frac{a}{1-a}\right). \quad (3)$$

This maps the interval  $[0, 1]$  onto the entire real number space  $(-\infty, +\infty)$ . For simplification, we denote the  $\text{logit}(a)$  as  $l_a$  in the following. The histogram for  $l_a$  is illustrated in Figure 7b, which resembles a normal distribution.

To support this statistically, we conducted a set of normality tests (Table 4) and show that for the raw accuracies, the null hypothesis should be rejected, while for the logits, we cannot reject the null hypothesis. This supports the use of effect size for the standardised comparisons that follow.



(a) Histogram of raw accuracy values with fitted Beta distribution.

(b) Histogram of logit-transformed accuracies with fitted normal distribution.

Figure 7: Histogram of accuracy on the uncorrupted datasets before and after logit transformation. (a) Accuracy values lie in the bounded interval  $[0, 1]$ , and those values for the uncorrupted set are usually very high, leading to a left-skewed distribution near 1. The fitted Beta distribution illustrates this skew. (b) After applying the logit transformation, the distribution becomes more symmetric, resembling a normal distribution. This transformation allows standardised comparisons using parametric methods.

	Shapiro–Wilk	D’Agostino–Pearson	Lilliefors
Accuracy ( $a$ )	0.004	0.001	0.021
Logit-transformed Accuracy ( $l_a$ )	0.194	0.135	0.192

Table 4: P-values from three normality tests (Shapiro–Wilk, D’Agostino–Pearson, and Lilliefors) applied to both raw accuracy values and logit-transformed accuracy. While the raw accuracy values significantly deviate from normality ( $p < 0.05$ ), the logit-transformed accuracies yield p-values above the 0.05 threshold across all tests. This indicates that we cannot reject the null hypothesis that  $l_a$  is drawn from a normal distribution.

## B. Formal Definitions of Error Alignment Metrics

This section provides complete definitions for the three behavioral alignment metrics used to characterise error patterns between classification systems.

Consider a dataset  $\mathcal{D} = \{(x_n, t_n)\}_{n=1}^N$  comprising inputs  $x_n \in \mathcal{X}$  and target labels  $t_n \in \mathcal{Y}$ , where  $\mathcal{Y}$  contains  $C$  classes. Let  $A$  and  $B$  denote two classification systems that produce predictions  $y_n^A$  and  $y_n^B$  respectively for each input  $x_n$ . Let  $p_A$  and  $p_B$  denote the accuracies of systems  $A$  and  $B$  on  $\mathcal{D}$ .

### B.1 Error Consistency (EC)

Error Consistency [13] measures the degree to which two systems produce correct or incorrect responses on the same stimuli, beyond what would be expected by chance given their individual accuracies.

First, we need to define the following instance counts on the dataset  $\mathcal{D}$ :

Do machines fail like humans?

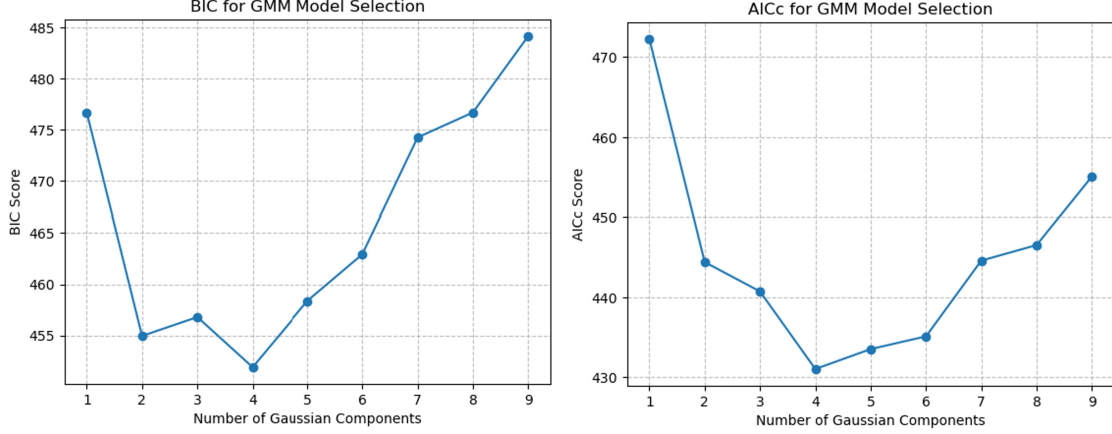


Figure 8: Model selection using the Bayesian Information Criterion (BIC) and corrected Akaike Information Criterion (AICc). Both criteria indicate four components as the optimal model complexity, with BIC and AICc reaching their minimum values at this point.

- $N_c$ : number of **jointly correct** instances where  $t_n = y_n^A = y_n^B$
- $N_e$ : number of *jointly incorrect* instances where  $y_n^A \neq t_n$  and  $y_n^B \neq t_n$

The *observed agreement rate* is the proportion of instances on which both systems agree in their correctness:

$$p_{\text{obs}} = \frac{N_c + N_e}{N} \quad (4)$$

The *expected agreement rate by chance*, assuming independence between the two systems' correctness, is:

$$p_{\text{exp}} = p_A \cdot p_B + (1 - p_A)(1 - p_B) \quad (5)$$

where  $p_A$  and  $p_B$  are the accuracies of systems  $A$  and  $B$  respectively.

Error Consistency is then defined as Cohen's kappa ( $\kappa$ ) computed over these values:

$$\text{EC}(A, B) = \frac{p_{\text{obs}} - p_{\text{exp}}}{1 - p_{\text{exp}}} \quad (6)$$

## B.2 Misclassification Agreement (MA)

Misclassification Agreement [14] quantifies alignment in the specific errors made when both systems misclassify the same stimuli, addressing the limitation that EC treats all joint errors identically regardless of the predicted classes.

The *error set* for a system  $g \in \{A, B\}$  is defined as as:

$$\mathcal{D}_g^{\text{err}} = \{(x_n, t_n) \in \mathcal{D} : y_n^g \neq t_n\}$$

The *joint error set* is the intersection:

$$\mathcal{D}_{A,B}^{\text{err}} = \mathcal{D}_A^{\text{err}} \cap \mathcal{D}_B^{\text{err}}$$

We then define the *error agreement matrix*  $M^{\text{err}} \in \mathbb{Z}_+^{C \times C}$  where the  $(i, j)$ -th element counts joint error instances with predictions  $y_n^A = i$  and  $y_n^B = j$ :

$$[M^{\text{err}}]_{ij} = |\{(x_n, t_n) \in \mathcal{D}_{A,B}^{\text{err}} : y_n^A = i, y_n^B = j\}|$$

Let  $N^{\text{err}} = |\mathcal{D}_{A,B}^{\text{err}}|$  denote the total number of joint errors.

Do machines fail like humans?

The *observed error-agreement rate* is the proportion of joint errors on which  $A$  and  $B$  predict the same (incorrect) class:

$$\tilde{p}_o = \frac{N_O^{\text{err}}}{N^{\text{err}}} = \frac{\sum_{i=1}^C [M^{\text{err}}]_{ii}}{N^{\text{err}}} \quad (7)$$

where  $N_O^{\text{err}}$  is the number of joint errors on which both systems agree (i.e., the trace of  $M^{\text{err}}$ ).

The *expected error-agreement rate by chance*, under the null hypothesis that predictions are independent on the joint error set, is:

$$\tilde{p}_e = \sum_{i=1}^C \hat{p}_i^{(A)} \cdot \hat{p}_i^{(B)} \quad (8)$$

where  $\hat{p}_i^{(g)}$  is the estimated probability that system  $g$  predicts class  $i$  on  $\mathcal{D}_{A,B}^{\text{err}}$ :

$$\hat{p}_i^{(A)} = \frac{\sum_{j=1}^C [M^{\text{err}}]_{ij}}{N^{\text{err}}}, \quad \hat{p}_i^{(B)} = \frac{\sum_{j=1}^C [M^{\text{err}}]_{ji}}{N^{\text{err}}} \quad (9)$$

(i.e., row and column marginals of  $M^{\text{err}}$  respectively).

Then, Misclassification Agreement is the multiclass Cohen's kappa of the error agreement matrix:

$$\text{MA}(A, B) = \kappa(M^{\text{err}}) = \frac{\tilde{p}_o - \tilde{p}_e}{1 - \tilde{p}_e} \quad (10)$$

### B.3 Class-Level Error Divergence (CLED)

Class-Level Error Divergence [14] measures the divergence of the distribution between the error patterns of two systems at the class level, without requiring instance-level correspondence. This enables comparison even when only aggregate confusion data is available.

For system  $g \in \{A, B\}$ , define the *error confusion matrix*  $F_g^{\text{err}} \in \mathbb{Z}_+^{C \times C}$  where the  $(i, j)$ -th element counts error instances with true class  $i$  and predicted class  $j$ :

$$[F_g^{\text{err}}]_{ij} = |\{(x_n, t_n) \in \mathcal{D}_g^{\text{err}} : t_n = i, y_n^g = j\}|$$

Note that diagonal elements  $[F_g^{\text{err}}]_{ii} = 0$  by construction (correct predictions are excluded).

For each true class  $i$ , collect the row of counts into vector  $\mathbf{f}_i^g = ([F_g^{\text{err}}]_{i1}, \dots, [F_g^{\text{err}}]_{iC})^\top$ . The *estimated error distribution* for system  $g$  on class  $i$  is computed as the expectation of a posterior Dirichlet distribution with prior  $\alpha \in \mathbb{R}_+^C$ :

$$\hat{\pi}_i^g = \frac{\mathbf{f}_i^g + \alpha}{\mathbf{1}^\top (\mathbf{f}_i^g + \alpha)} \quad (11)$$

where  $\mathbf{1}$  is the vector of all ones. A symmetric prior  $\alpha = 0.5 \cdot \mathbf{1}$  (Jeffreys prior) is typically used.

The Jensen-Shannon Divergence (JSD) between two probability distributions  $P$  and  $Q$  is:

$$\text{JSD}(P, Q) = \frac{1}{2} D_{\text{KL}}(P \| M) + \frac{1}{2} D_{\text{KL}}(Q \| M) \quad (12)$$

where  $M = \frac{1}{2}(P + Q)$  is the mixture distribution and  $D_{\text{KL}}$  denotes the Kullback-Leibler divergence:

$$D_{\text{KL}}(P \| Q) = \sum_i P(i) \log \frac{P(i)}{Q(i)} \quad (13)$$

JSD is symmetric, bounded in  $[0, 1]$  (when using  $\log_2$ ), and well-defined even when distributions have zero entries.

The *Class-Level Error Divergence* aggregates JSD across all classes with sample-size weighting:

$$\text{CLED}(A, B) = \sum_{i=1}^C w_i \cdot \text{JSD}(\hat{\pi}_i^A, \hat{\pi}_i^B) \quad (14)$$

where the weight  $w_i$  for class  $i$  is the proportion of total errors (across both systems) with ground-truth class  $c$ , normalised by the total number of errors:

$$w_i = \frac{n_i^A + n_i^B}{\sum_{j=1}^I (n_j^A + n_j^B)} \quad (15)$$

C. Patterns for Error Alignment

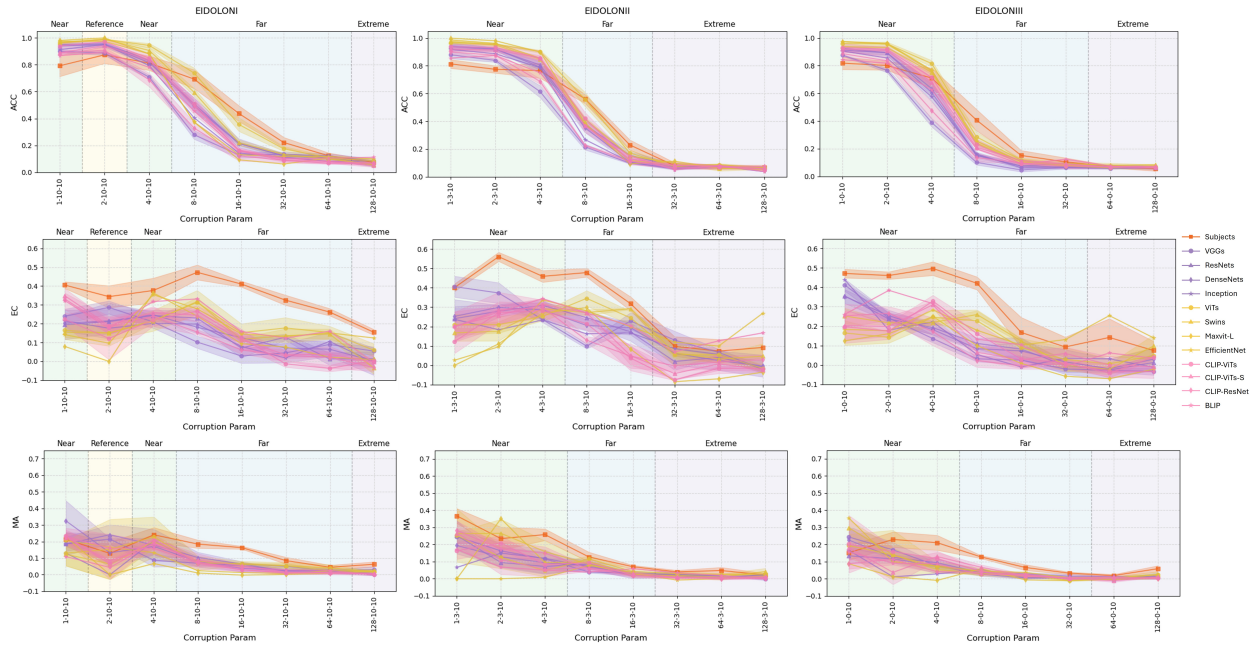


Figure 9: Accuracy (ACC, top row), Error Consistency (EC, middle row), and Misclassification Agreement (MA, bottom row) for humans and models across three distortion types: EidolonI (left), EidolonII (middle), EidolonIII (right).

# Do machines fail like humans?

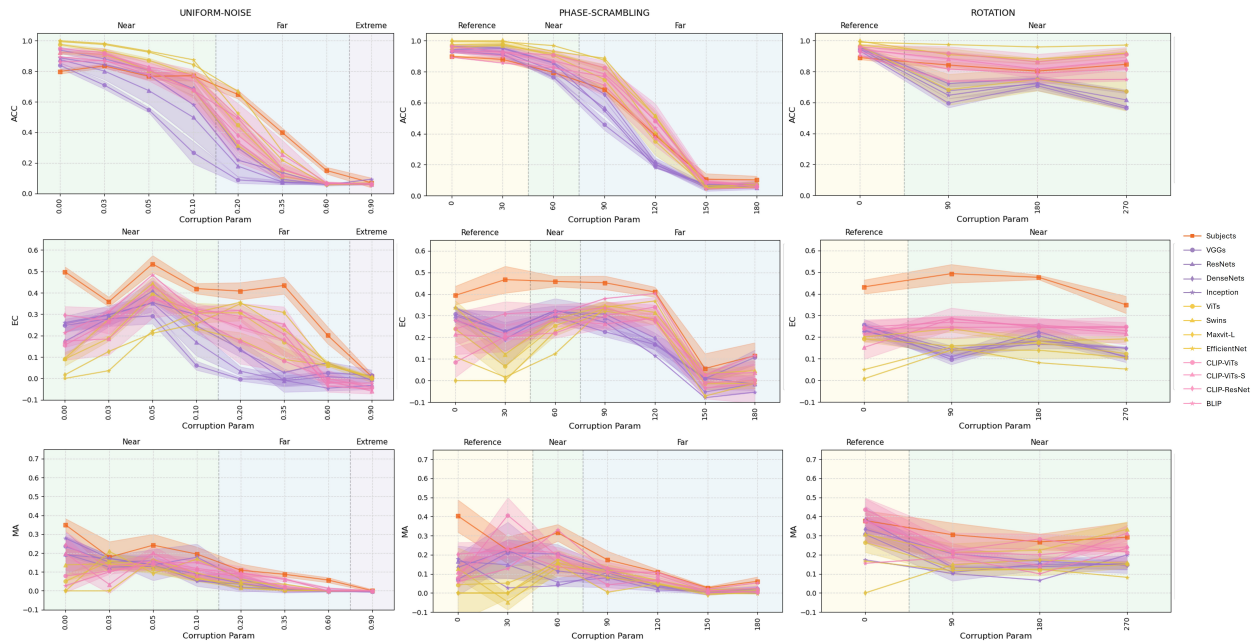


Figure 10: Accuracy (ACC, top row), Error Consistency (EC, middle row), and Misclassification Agreement (MA, bottom row) for humans and models across three distortion types: Uniform Noise (left), Phase Scrambling (middle), Rotation (right).

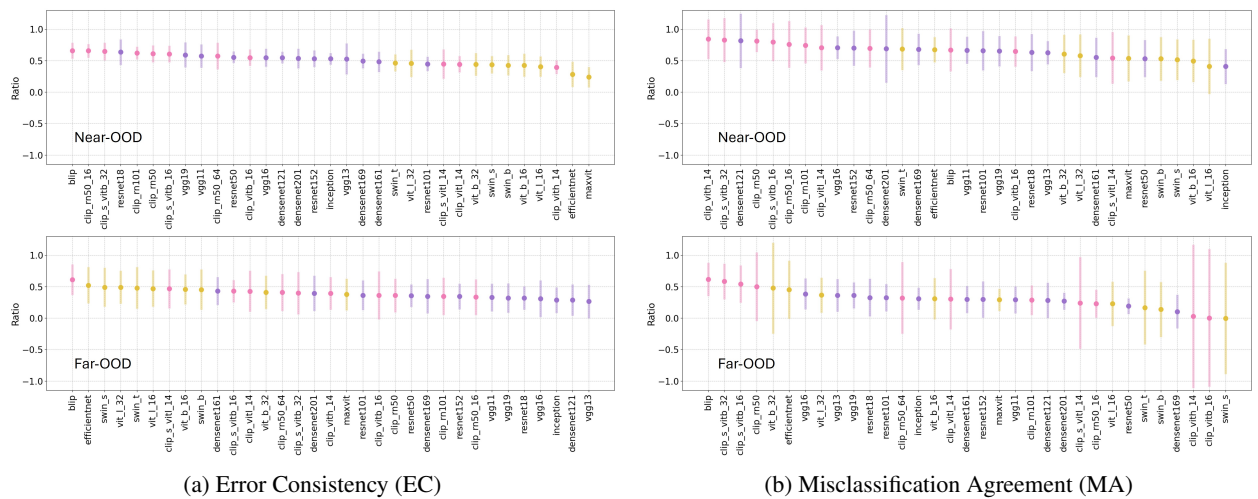


Figure 11: The ranking for each metric.

Do machines fail like humans?

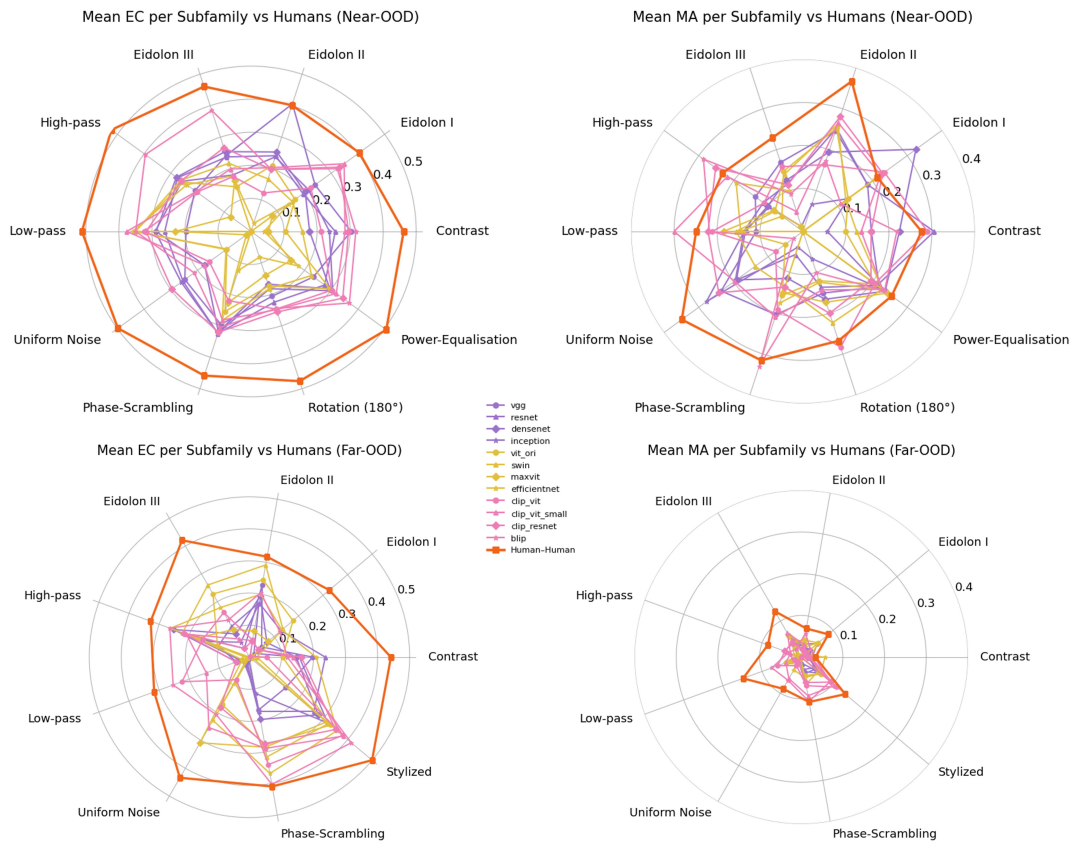


Figure 12: Radar plots of mean model–human error alignment for each subfamily across distortion types, separated by OOD regime (near-OOD, EC (left top), MA (right top); far-OOD, EC (left bottom), MA (right bottom)). Human–human alignment scores are denoted in orange.